Chapter 3

Study of luminescence properties in Li^+ ion co-doped Bi_2O_3: Sm^{3+} nano-sheets

This chapter presents a report on the correlation between structural, morphological, and luminescence properties of a series of Sm^{3+} (1-7 mol %) doped and Li^+ (0.5-3 mol %) co-doped Bi_2O_3 nano-sheets synthesized via co-precipitation method. The X-ray diffraction (XRD) study ascertains monoclinic phase of the prepared samples. An improved crystalline nature and reduced strain upon Li^+ co-doping was observed. X-ray photoelectron spectroscopy (XPS) explores the chemical composition and oxidation state of the elements present in the sample surface. The UV- Vis spectroscopy has been implemented to investigate the band gap of the samples. An increment is observed in the band gap upon doping as well as co-doping. The photoluminescence (PL) emission spectrum was recorded at 481 nm excitation, over the range of 540-740 nm. Two-fold enhancement in the emission intensity of the Li^+ co-doped samples has been recorded as compared to the Sm^{3+} doped Bi_2O_3 samples which make the phosphors worthy to be served as exquisite candidates to realize efficient warm white light emitting diodes (wLEDs).

3.1 Introduction

Over the last few years, white light emitting diodes (wLEDs) have surged increasing amount of interest owing to their noteworthy and remarkable features such as extraordinary luminous efficiency, high durability, longer lifetime, low power consumption, and eco-friendly nature [42–44] and have found multifarious commercial and potential applications in X-ray imaging, optical communications, lighting and display devices, etc., [45,46]. In addition, wLEDs are beneficial over numerous harmful effects such as eye-straining and headache problems caused by the poor lighting of Incandescent bulbs and fluorescent lamps.

There are predominantly three technologies through which wLEDs are produced such as wavelength conversion, colour mixing, and homo-epitaxial ZnSe technology. Among them, wavelength conversion is a prevalent and used technology, in which a yellow or red-emitting phosphor is coated over a blue chip to realize wLEDs. However, the commercially available wLEDs (blue GaN-based cerium-doped $Y_3Al_5O_{12}$ (YAG: Ce^{3+}) yellow emitting phosphors) are abided by poor color rendering index ($CRI < 80$), high color temperature ($CCT > 5000$) values, and poor illumination and thus, their practical implications are restrained owing to the lack of red component [43–45]. Therefore the red component is indispensable to overcome these problems and for realizing the efficient warm white light emitting diodes.

Rare earth (Ln^{3+}) doped metal oxide phosphors have been widely studied owing to their unique and unprecedented optical properties such as excellent color purity, longer excited-state lifetime, quantum efficiency, and chemical stability arising due to intra configurational 4f-4f transitions and have been extensively employed as activator ions for various phosphors[47,48].

Several attempts have been made to enhance the luminescence intensity of rare earth (Ln^{3+}) doped metal oxide phosphors. Bae *et al.* [49] have prepared Li-doped Y_2O_3:Eu^{3+} thin film phosphors via pulsed lased deposition technique. P. Kumar *et al.*[50] have synthesized Li^+ ion assisted Eu-doped ZnO via sol-gel method. A. K. Singh *et al.* [51] have discussed the crucial role played by Li^+ ions as co-activators in the luminescence enhancement of Ln^{3+} ions.

Among several rare-earth doped metal oxides nanophosphors (MNPs), Sm^{3+} doped Bi_2O_3 nanophosphors have drawn huge attention because of their intriguing and ubiquitous features such as non-toxicity, large oxygen ion conductivity, high refractive index, exquisite light absorbing properties, and extraordinary photocatalytic and luminescence properties [52–54] and leads to a plethora of applications in the diverse arena such as fuel cells, catalysts, solar cells, gas sensors, and electronic devices [55]. Bi_2O_3 exists mainly in five polymorphic phases namely, α (monoclinic), β (tetragonal), γ (body-centered cubic), δ (face-centered cubic), and ω (triclinic). Among them, the monoclinic phase α-Bi_2O_3 shows the room temperature stability [56]. Sm^{3+} ion is extensively employed as a prominent activator ion in various host lattices due to its reddish-orange emission owing to $^4G_{5/2}$→ ^6H_J transitions (J = 5/2, 7/2, 9/2, 11/2), and therefore Sm^{3+} doped phosphor materials are regarded as suitable candidates for wLED applications [46,57].

This chapter describes the influence of Li^+ co-doping on structural, morphological, optical and luminescence properties of Sm^{3+} doped Bi_2O_3 nano-sheets, synthesized via a simple, viable, cost-effective, facile, and room temperature co-precipitation method. Furthermore, it presents a correlation between the structural, morphological, and luminescence properties of the synthesized nano-sheets.

3.2 Experimental Procedure

3.2.1 Materials

Bismuth nitrate pentahydrate [$Bi(NO_3)_3 \cdot 5H_2O$, 98%, Sigma-Aldrich], samarium nitrate ($Sm(NO_3)_3$, 99.999%, Sigma-Aldrich), lithium acetate [$CH_3COOLi \cdot 2H_2O$, 99%, Molychem], sodium hydroxide (NaOH, 98%, Sigma-Aldrich).

3.2.2 Synthesis of Sm^{3+}/Li^+ co-doped Bi_2O_3 nano-sheets

Bismuth oxide (Bi_2O_3) and Sm^{3+}/Li^+ co-doped bismuth oxide nano-sheets were synthesized via co-precipitation method. We have synthesized Bi_2O_3, Sm (1-7 mol %) doped Bi_2O_3 and Sm (5 mol %) doped, Li (0.5, 1, and 3 mol %) co-doped Bi_2O_3 nanosheets. The samples are specified with code names BS0, S1, S3, S5, S7, SL0.5, SL1, and SL3, respectively. Briefly, a stoichiometric amount of bismuth nitrate pentahydrate was taken in a beaker with 10 ml DI water on a magnetic stirrer at 50 ^oC. Few drops of HNO_3 were added to get a clear transparent solution. Required amount of samarium nitrate was added with constant stirring. In another beaker stoichiometric proportion of lithium acetate was taken and concentrated nitric acid was added drop-wise for 3-4 hrs. Heating was continued to remove excess acid. Both the solutions were then transferred in a single beaker and the stirring was continued to ensure the proper mixing. 2M NaOH was added drop-wise to ensure complete precipitation. The stirring was continued for another 20-30 minutes and thereafter the reaction mixture was left overnight for sedimentation. The white precipitate thus obtained was washed several times with DI water for the complete removal of any existing contaminant and then dried in an air oven at 80 ^oC overnight. The obtained white powder was calcined in air at 600 ^oC for 4hrs. The resultant bright yellow powder was then characterized. Same procedure was followed to synthesize the undoped Bi_2O_3 but without adding the dopants.

3.3 Characterizations

Rigaku Miniflex 600 Desktop X-Ray Diffraction System facilitated with monochromatic Cu K_α radiation (λ=1.54 Å) was used to confirm the phase formation and the determination of crystal structure of the synthesized samples. The continuous scanning mode diffraction spectra were recorded at the intervals of 0.02^o ranging from $20^o \leq 2\theta \leq 70^o$. X-ray photoelectron spectrum has been recorded with Thermo Fisher Scientific X-ray photoelectron spectrometer using monochromatic Al K_α source (1486.7 eV). JASCO V770 UV-Vis-NIR spectrophotometer was probed to analyze the Optical absorption spectra in the range of 200 nm - 1000 nm. JASCO FT/IR 4600 spectrometer was used as a tool to examine the Fourier transform infrared spectra (FTIR) for chemical bonding and functional group analysis over the range of 400 cm^{-1} - 4000 cm^{-1}. The study of surface morphology and the estimation of thickness of nano-sheets were carried out using high-resolution scanning electron microscopy (HR-SEM) (Nova Nano SEM 450, FEI Company of USA (S.E.A.) PTE, LTD). The energy-dispersive X-ray (EDX) spectroscopy was performed along with the HR-SEM analysis to corroborate the presence of each element and to validate their estimated proportions used in the synthesis process. Fluorolog-3 spectrofluorometer, HORIBA Instruments Inc. equipped with a 450-W Xe-flash lamp was used to measure the photoluminescence (PL) excitation and emission spectra.

3.4 Results and discussion

3.4.1 X-ray diffraction analysis

The X-ray diffraction (XRD) analysis was performed to authenticate the phase purity and to determine the crystal structure of the synthesized samples. Fig. 3.1 (a) depicts the XRD patterns of BS0, S5, and SL (0.5-3) nano-sheets, calcined at 600 ^oC . The XRD spectra ascertain the monoclinic phase of the prepared nano-sheets. All the peaks were indexed

according to the standard Bragg's positions (JCPDS file no. 41-1449) and match well with the monoclinic structure of Bi_2O_3. The XRD patterns of Sm^{3+} doped and Sm^{3+}/Li^+ co-doped samples exhibit some small impurity peaks corresponding to bismuth samarium oxide [marked as * in Fig. 3.1 (a)]. However, the intensity of these impurity peaks decreases gradually on increasing the Li concentration in co-doped samples, which can be attributed to the better crystallization upon Li co-doping [58,59].

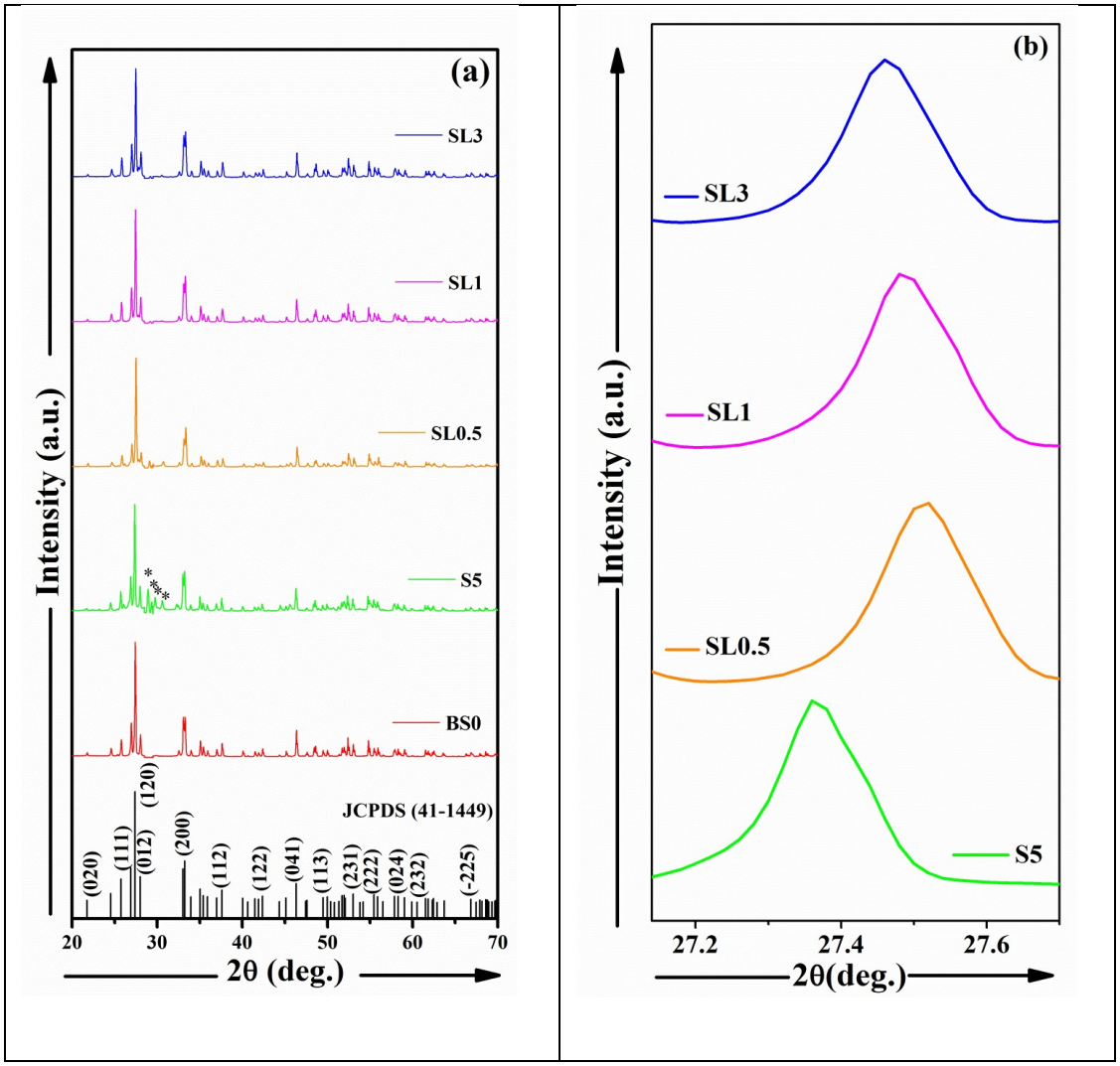

Fig. 3.1 (a) Stacked XRD patterns of BS0, S5, and SL (0.5- 3 mol%) and **(b)** Magnification of the (120) peak Shift in S5, and SL (0.5- 3 mol%).

The average crystallite size (L) of the prepared nano-sheets has been estimated using the well-established Debye- Scherrer formula.

$$L = \frac{K\lambda}{\beta \cos\theta} \tag{3.1}$$

Where β is full width at the half-maximum (FWHM in radians), θ is corresponding Bragg's angle, K is shape factor (~ 0.9) and λ is the incident X-ray wavelength (λ = 0.154 nm). However, the Scherrer formula does not involve the peak broadening arising due to the strain component (ε). Therefore, the average crystallite size, as well as strain values have been estimated using Williamson- Hall (W-H) formula [60,61],

$$\beta \cos\theta = 4\varepsilon \sin\theta + \frac{K\lambda}{L} \tag{3.2}$$

In W-H plot, $\beta \cos\theta$ is plotted against $4\varepsilon \sin\theta$ and fitted linearly. The y-axis intercept of this linear fit provides the crystallite size and the slope of this curve gives the strain values. The variation in crystallite size and lattice strain values of the synthesized nano-sheets using Williamson-Hall method is displayed in Fig. 3.2 and the obtained values are tabulated in Table 3.1. An augmentation in the crystallite size is observed upon Li^+ co-doping in Bi_2O_3:Sm^{3+} doped samples which suggests an improvement in the crystalline nature of the co-doped samples. As the ionic radius of Li^+ ions (0.76Å) is smaller than the Bi^{3+} ions (1.03Å), it is easily incorporated in the host lattice. For the lower co-doping concentration (SL0.5) of Li^+ ions in Bi_2O_3:Sm^{3+} lattice, we observe a shift in the peak position of the most intense peak towards the higher angle side (Fig. 3.1 (b)), which can be attributed to the substitution of Li^+ ions at the Bi^{3+} sites and results in the reduction of crystal cell volume and an increase in the full width at half maximum (FWHM). As a result, the crystallite size decreases. On the other hand, as we further increase the Li^+ co-doping concentration the extra Li^+ ions start occupying the interstitial

positions. Consequently, the peak position starts shifting towards the lower angle side and leads to the expansion in the crystal cell volume and a decrease in the FWHM. Thus, the crystallite size increases and the crystallinity is improved [54,62–64]. This phenomenon may give rise to the creation of a significant amount of unoccupied sites in the oxygen ion array and may lead to the expansion of lattice and hence the reduction in crystal density, as a result, the crystallinity is improved [59,65]. Furthermore, with the increase in size of crystallites the grain boundary density is reduced which further reduces the available light adsorption or scattering sites, as a result of which the luminescence is enhanced [61]. Moreover, a decrease in the observed lattice strain values upon Li co-doping suggests the reduced crystal defects and improved local ordering of the crystal structure, which is also favourable for the enhancement in the luminescence intensity [66].

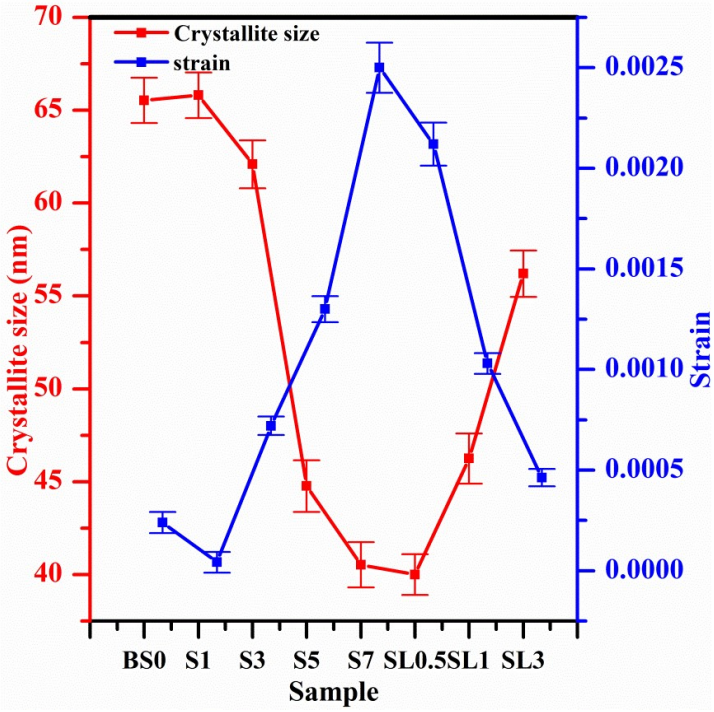

Fig. 3.2 Variation of crystallite size (***L***) and strain (***ε***) with dopant concentrations.

Table 3.1 Crystallite size (L) and strain (ε) values of all samples.

Sample	Debye- Scherrer method	Williamson- Hall method	
	Crystallite size (nm)	Crystallite size (nm)	Strain
BS0	65.05	65.53	2.39×10^{-4}
S1	60.37	65.81	4.18×10^{-5}
S3	59.05	62.09	7.2×10^{-4}
S5	58.37	44.77	1.3×10^{-3}
S7	49.83	40.52	2.5×10^{-3}
SL0.5	59.11	40	2.12×10^{-3}
SL1	58.56	46.25	1.03×10^{-3}
SL3	60.01	56.20	4.63×10^{-4}

3.4.2 XPS analysis

The chemical composition and oxidation state of the elements present in the sample surface were investigated by X-ray photoelectron spectroscopy (XPS) analysis. The binding energies of elements were calibrated using C 1s (284.7 eV) as the reference peak [67]. After Shirley-type background subtraction the peaks have been fitted with Gaussian-Lorentzian peak shapes using the XPSPEAK41 software. Fig. 3.3 (a) depicts the XPS survey scan of SL1 sample and the peaks corresponding to Bi, Sm, Li and O ascertain the presence of all elements in the sample. The XPS spectrum of Li 1s is shown in Fig. 3.3 (b). The observed peak at 55.2 eV corresponds to Li^+ oxidation state and confirms the

presence of Li in the sample [68]. Fig. 3.3 (c) shows the XPS spectra of Bi 4f core level. The spectra exhibit two prominent peaks centered at 158.9 and 164.2 eV binding energies corresponding to Bi $4f_{7/2}$ and Bi $4f_{5/2}$ of Bi^{3+} ion in the sample, respectively [54]. The O 1s core level XPS spectra (Fig. 3.3 (d)) shows asymmetric nature and therefore, it is deconvoluted into four peaks centered at 529.5, 530.9, 531.5 and 532.5 eV, which are attributed to the lattice oxygen ion of Bi-O bonding, oxygen vacancies (V_o), adsorbed surface oxygen due to the presence of hydroxyl (-OH) groups and O-C=O bonds, respectively [54,67,69]. In addition, the peaks centered at 1082.7 and 1110.2 eV in Fig. 3.3 (e) are assigned to Sm $3d_{5/2}$ and Sm $3d_{3/2}$, respectively [54]. These results confirm the +3 oxidation state of Sm.

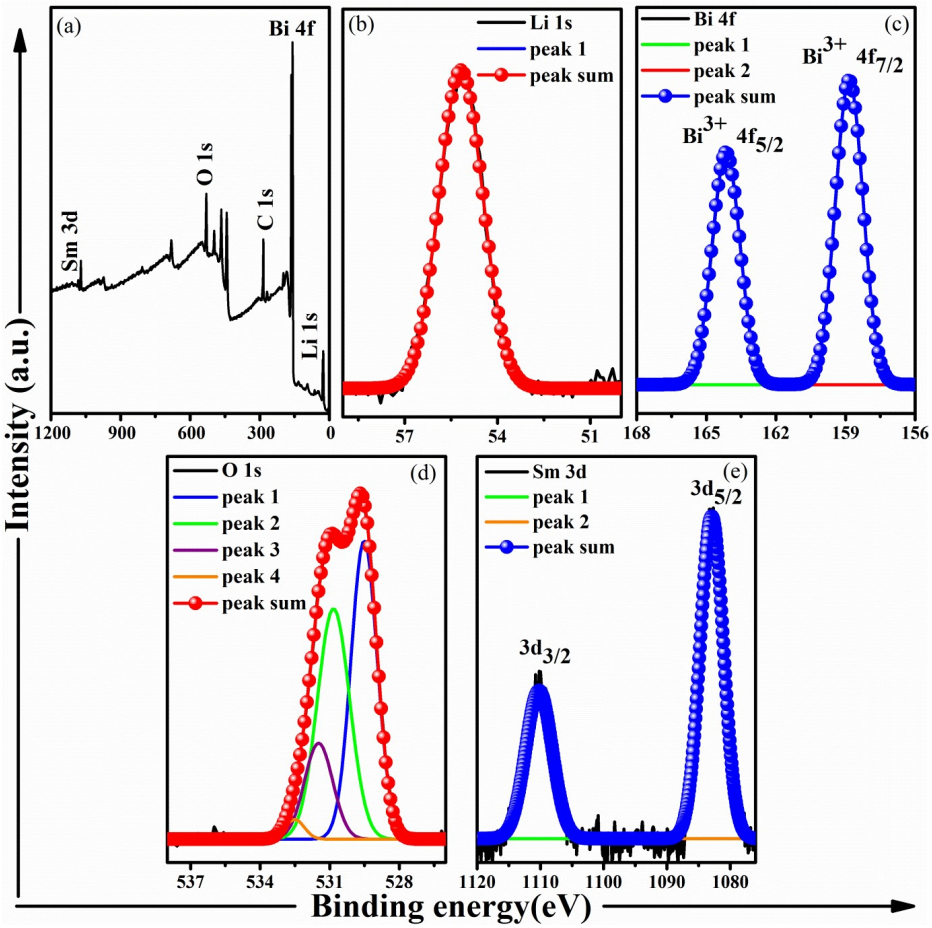

Fig. 3.3 (a) XPS survey scan, and high resolution XPS spectra of **(b)** Li 1s **(c)** Bi 4f **(d)** O 1s and **(e)** Sm 3d for SL1 sample.

3.4.3 Optical absorption and band gap analysis

The optical absorption spectra of the prepared samples accomplished over the wavelength range of 200-1000 nm are shown in Fig. 3.4 (a). The optical band gap (E_g) of the samples have been evaluated using the well-known Tauc relation [70],

$$(\alpha h\nu)^2 = B(h\nu - E_g) \qquad (3.3)$$

Where B is a constant, $h\nu$ represents the energy of incident photon and the absorption coefficient is denoted by α. The corresponding Tauc plot is displayed in Fig. 3.4 (b) and the obtained band gap values are tabulated in Table 3.2. The Sm^{3+} doping as well as the Li^+ co-doping in the Bi_2O_3 creates ample carrier concentration and leads to the upliftment

of Fermi level into the conduction band. Consequently, an apparent blue shift in the absorption edge or shift of the band gap towards the higher energy side is observed, which is attributed to the Burstein-Moss effect [71]. A slight increment in the band gap value suggests the lowering of defect states or disorders within the band gap region, which in turn improves the crystallinity of the samples [72].

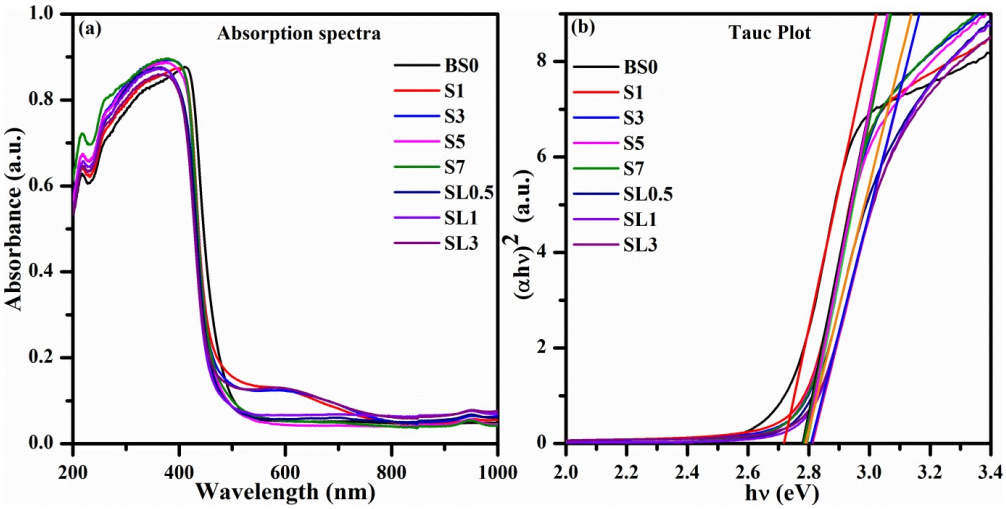

Fig. 3.4 (a) UV-Vis absorption spectra and **(b)** Tauc plot of all the samples.

The Urbach energy (E_U) elucidates the width of localized states tail in the optical band gap region created by the defect states. The empirical Urbach rule is given by the formula[73],

$$\alpha = \alpha_o e^{(\frac{h\nu}{E_U})} \tag{3.4}$$

Where α_o is a constant and the inverse of the slope of the linear part of $\ln(\alpha)$ vs $h\nu$ plot gives the Urbach energy. The estimated results are summarized in Table 3.2. The Urbach energy values decrease with increasing the dopant concentrations and clearly validate the obtained band gap results [74]. The variation in band gap and Urbach energy with the dopant concentrations are depicted in Fig. 3.5. The presence of oxygen vacancies can be confirmed from the observed XPS results of the SL1 sample. However, at higher co-

doping concentration (SL3), there may be creation of a large amount of oxygen vacancies, which may result in the formation of additional defect or localized states and lead to the reduction in optical band gap and an increase in the Urbach energy [75].

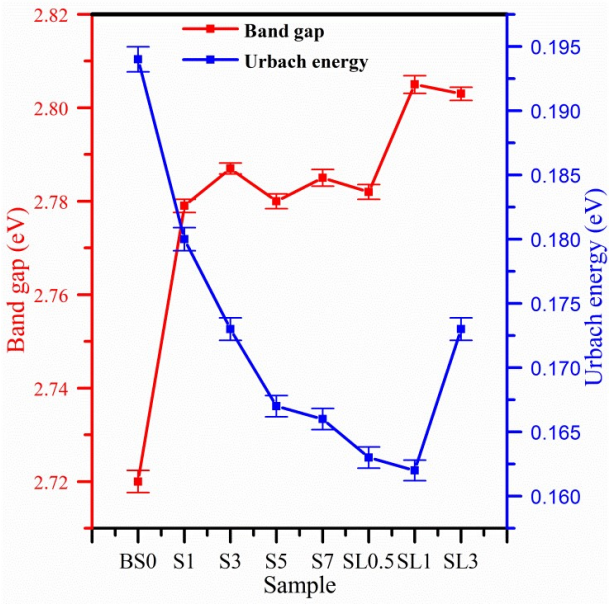

Fig. 3.5 Variation of band gap (E_g) and Urbach energy (E_U) values with dopant concentrations.

Table 3.2 Band gap (E_g) and Urbach energy (E_U) values of the samples.

Sample	**Band gap (E_g) (eV)**	**Urbach Energy (E_U) (eV)**
BS0	2.720	0.194
S1	2.779	0.180
S3	2.787	0.173
S5	2.780	0.167
S7	2.785	0.166
SL0.5	2.782	0.163
SL1	2.805	0.162
SL3	2.803	0.173

3.4.4 FTIR analysis

The room temperature FTIR analysis of the synthesized nano-sheets has been performed over the range of 400-4000 cm^{-1}, to investigate the chemical bonding and to substantiate the presence of functional groups. Fig. 3.6 illustrates the FTIR spectra of BS0, S5, and SL1, respectively. The peaks near 440 and 660 cm^{-1} are attributed to the characteristic absorption bands corresponding to Bi-O stretching vibrations [76,77]. The peak centered at 2360 cm^{-1} corresponds to the stretching vibration of CO_2 molecule [70] while the broadband around 1340-1360 cm^{-1} arises due to the existence of nitrate ions and suggests the presence of NO_3^- functional group [78,79]. The IR bands around 1660 and 2998 cm^{-1} are assigned to the C=O stretching and asymmetric C-H stretching, respectively [80].

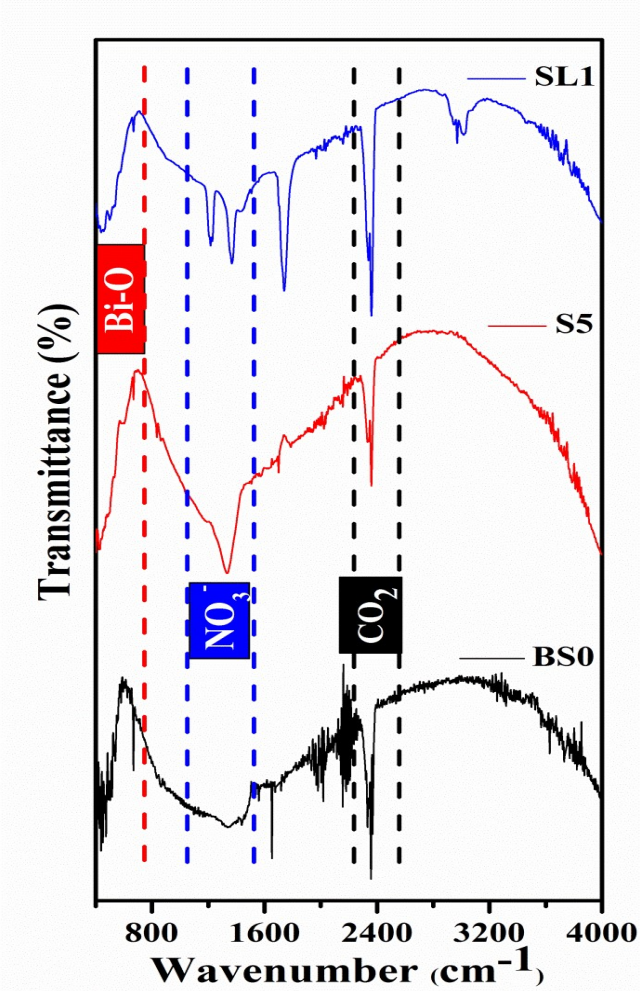

Fig. 3.6 FTIR spectra of BS0, S5, and SL1.

3.4.5 Morphological and elemental analysis

The morphological analysis of the samples has been done using HR-SEM micrographs, shown in Figs. 3.7 (a-e), which ascertains the nano-sheet like structure of the prepared samples. Average thickness of the nano-sheets was computed using ImageJ software and the results are summarized in Table 3.3. From the observed results, we can infer that the thickness of nano-sheets increases upon increasing the Li^+ ion concentration thereby increasing the number of adsorbed oxygen on the surface of nano-sheets and hence the concentration of luminescence quenching centres are reduced and emission intensity is improved [80,81]. However, with the increase in Li^+ co-doping concentration, the emission

intensity increases up to a certain extent (SL1) and decreases on further increasing the co-doping concentration. The reduction in the emission intensity of the co-doped samples after the critical Li concentration may be attributed to the concentration quenching. The discussion on the reasons for concentration quenching is done later in the photoluminescence section.

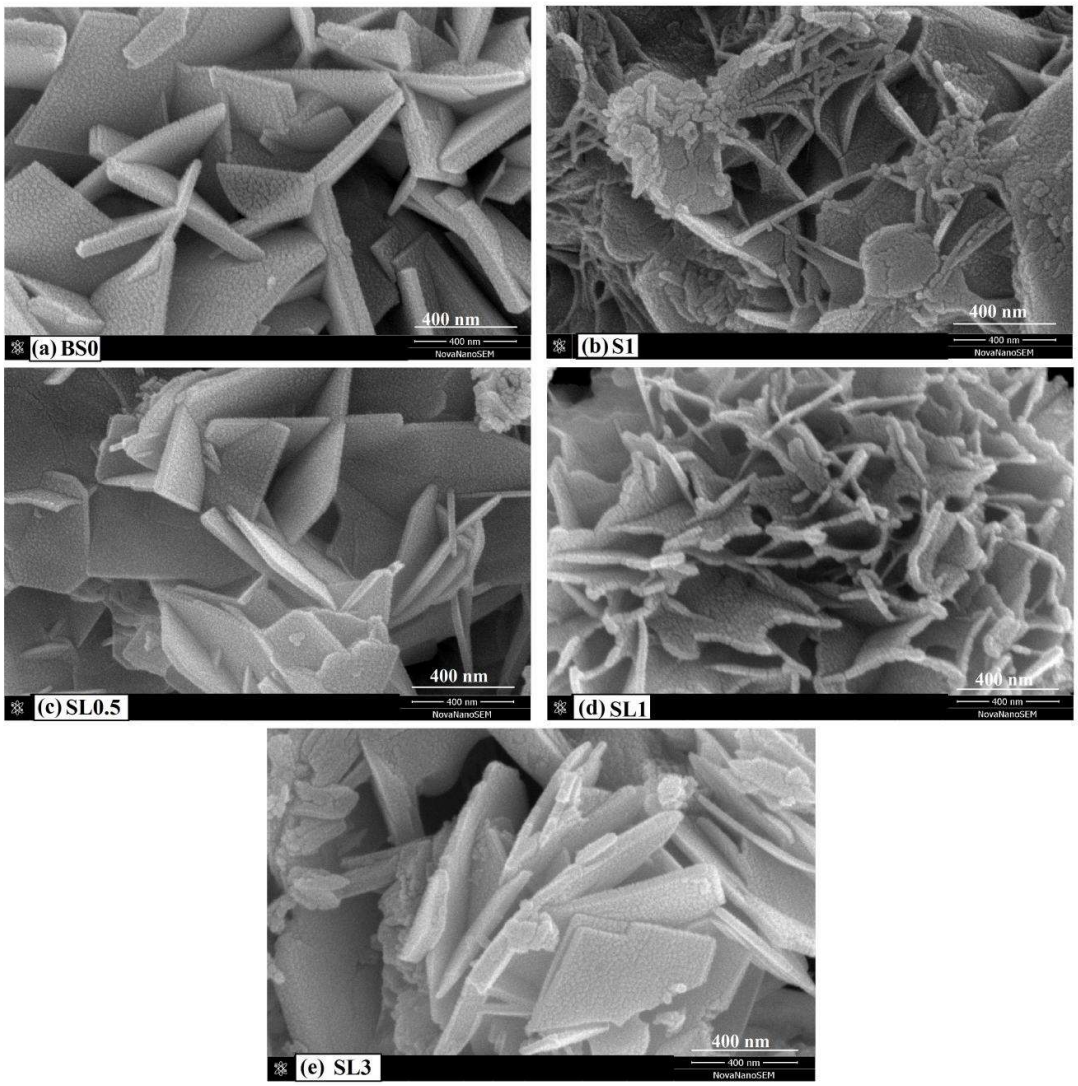

Fig. 3.7 HR-SEM micrographs of **(a)** BS0, **(b)** S1, **(c)** SL0.5, **(d)** SL1 and **(e)** SL3, respectively.

Table 3.3 Average thickness of the synthesized nano-sheets.

Sample name	Average thickness (nm)
BS0	51.00
S1	29.10
SL0.5	31.47
SL1	35.62
SL3	37.97

Furthermore, the existence of each element and their estimated proportions used in the synthesis process has been verified by EDX spectra, depicted in Fig. 3.8. Small peaks of Au are also present in the spectra, arising due to the conductive coating used during sampling. However, due to the limitation of the instrument, Li is not detected in EDX analysis. The atomic % and weight % of the elements present in BS0 and S7, as obtained from EDX spectra and their estimated amounts are summarized in Table 3.4 and found in agreement with each other.

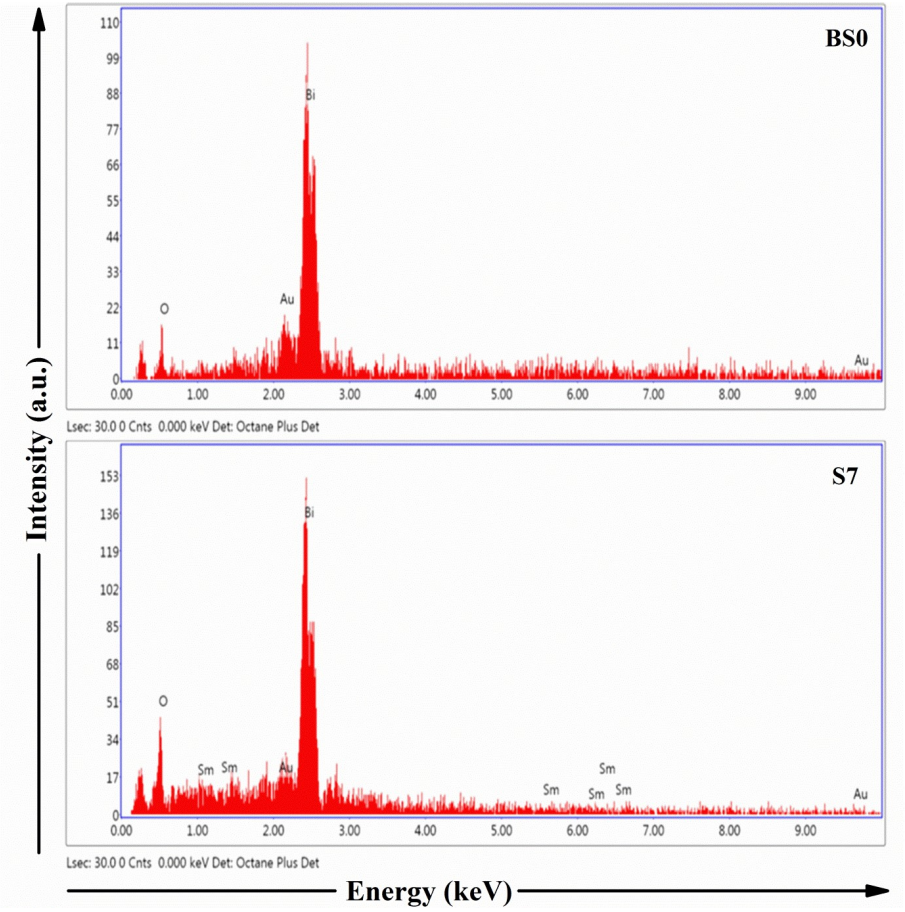

Fig. 3.8 Energy dispersive X-ray (EDX) spectra of BS0 and S7 nano-sheets.

Table 3.4 Atomic % and weight % of BS0 and S7 obtained from EDX data and estimated amount used in the synthesis process.

Sample	**Elements**	**Estimated amount**		**Obtained from EDX**	
		At. %	Wt.%	At. %	Wt.%
BS0	Bi	40	89.70	36.84	81.45
	O	60	10.30	59.06	10.00
S7	Bi	38.6	87.33	21.05	68.76
	Sm	1.4	2.28	1.99	4.67
	O	60	10.39	74.37	18.59

3.4.6 Photoluminescence study

The nanosized Bi_2O_3 exhibits photoluminescence due to quantum confinement and structural defects in the crystal [82]. The photoluminescence excitation (PLE) and emission spectra of Bi_2O_3 are depicted in Figs. 3.9 (a) and (b), respectively. The PLE spectrum was recorded at an emission wavelength of 442 nm ranging from 250-400 nm. The broadband centered around 380 nm is accredited to ligand (O^{2-}) to metal (Bi^{3+}) charge transfer (LMCT) band arising due to transfer of electrons from occupied 2p orbital of O^{2-} to the Bi^{3+} ions or intraionic transition of Bi^{3+}. The emission peak corresponding to 370 nm excitation and centered at 442 nm is designated to the $3_{P_1} \rightarrow 1_{S_0}$ transition of Bi^{3+} ion [55,83,84].

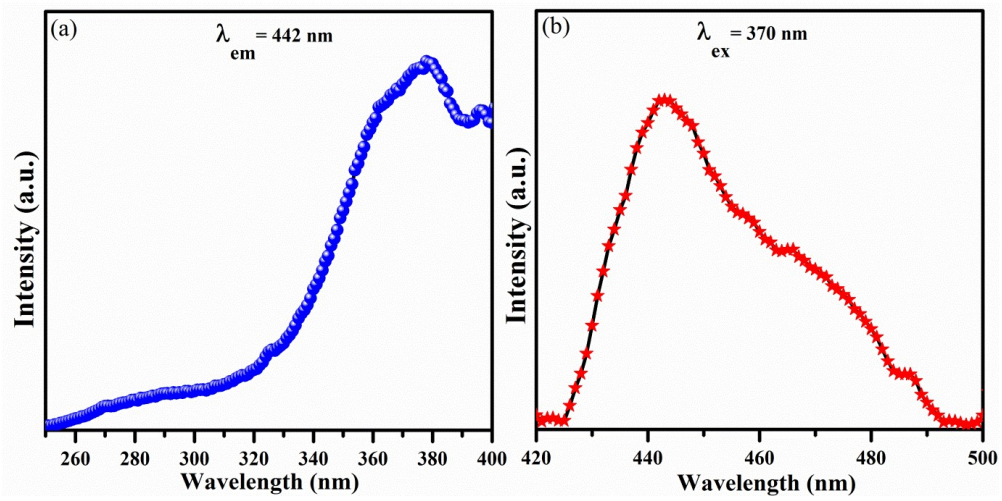

Fig. 3.9 (a) PL excitation (PLE) and (b) PL emission spectra of Bi_2O_3 host.

The PL excitation spectra (PLE) of Bi_2O_3:Sm^{3+} and Bi_2O_3 :($Sm3^+$, Li^+), taken in the range 360 nm-500 nm are shown in Figs. 3.10(a) and (b), respectively. The spectra exhibit bands at 366 nm ($6_{H_{5/2}} \rightarrow 4_{D_{\frac{3}{2},\frac{5}{2}}}$), 406 nm ($6_{H_{5/2}} \rightarrow 4_{F_{7/2}}$), 450 nm ($6_{H_{5/2}} \rightarrow 4_{G_{9/2}}$), 467 nm ($6_{H_{5/2}} \rightarrow 4_{I_{13/2}}$), 474 nm ($6_{H_{5/2}} \rightarrow 4_{I_{11/2}}$), and 481 nm ($6_{H_{5/2}} \rightarrow 4_{I_{9/2}}$), attributed to

the 4f-4f transition of Sm^{3+} [35]. Among these, the most intense transition ($6_{H_{5/2}} \rightarrow 4_{I_{9/2}}$) was observed at 481 nm and was used to explore the emission spectra.

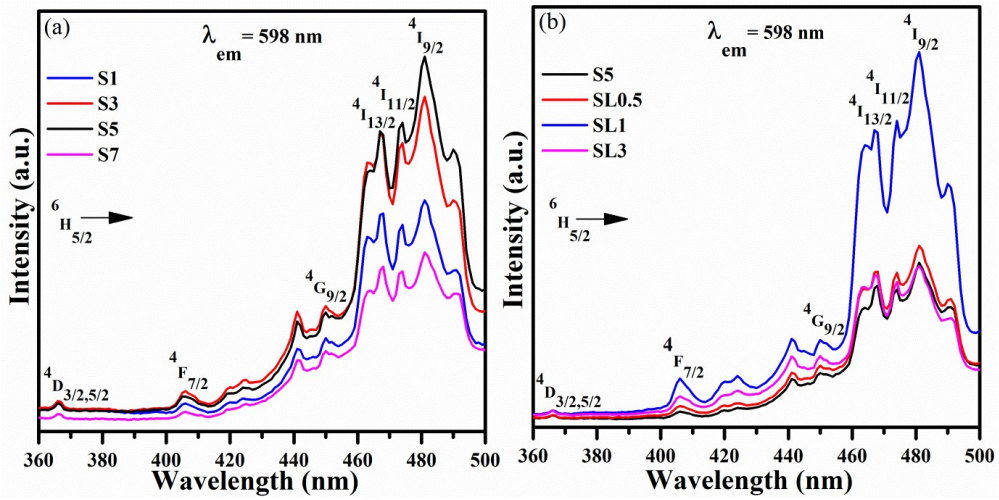

Fig. 3.10 PL excitation (PLE) spectra of **(a)** $Bi_2O_3:Sm^{3+}$ and **(b)** $Bi_2O_3:(Sm^{3+}, Li^+)$ samples.

Figs. 3.11 (a) and (b) Show the room temperature emission spectra of $Bi_2O_3:Sm^{3+}$ and Bi_2O_3 :(Sm^{3+}, Li^+) at an excitation wavelength of 481 nm ($6_{H_{5/2}} \rightarrow 4_{I_{9/2}}$), respectively. The spectra consist of emission bands at 562 nm ($4_{G_{5/2}} \rightarrow 6_{H_{5/2}}$), 598 nm ($4_{G_{5/2}} \rightarrow 6_{H_{7/2}}$), and 645 nm ($4_{G_{5/2}} \rightarrow 6_{H_{9/2}}$), respectively. Among these, the 562 nm ($4_{G_{5/2}} \rightarrow 6_{H_{5/2}}$) transition is ascribed to the magnetic dipole transition, which is less sensitive to the crystal field environment whereas the 645 nm ($4_{G_{5/2}} \rightarrow 6_{H_{9/2}}$) transition is attributed to the hypersensitive electric dipole transition and its intensity strongly depends on the crystal field environment. The strongest emission peak was observed at 598 nm ($4_{G_{5/2}} \rightarrow 6_{H_{7/2}}$) which is partially electric and partially magnetic dipole transition and corresponds to the orange-reddish emission of the phosphor [85].

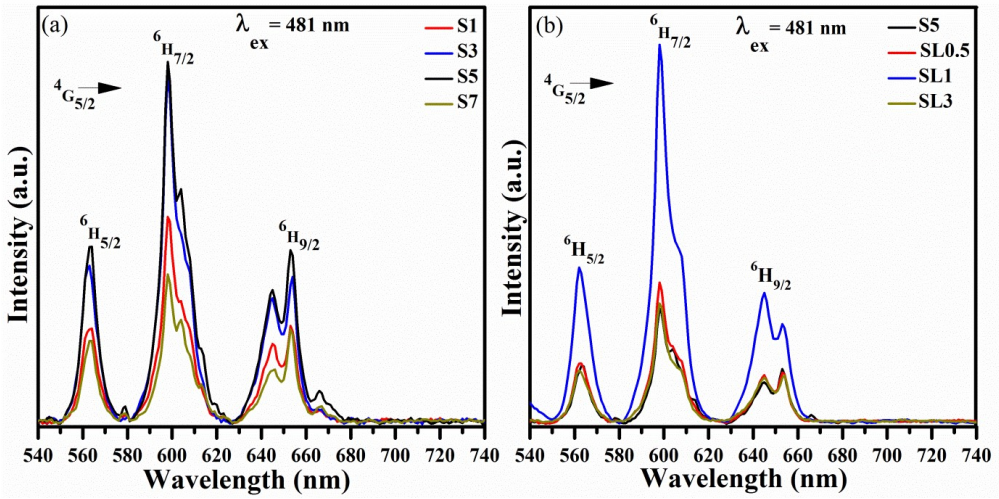

Fig. 3.11 PL emission spectra of **(a)** $Bi_2O_3:Sm^{3+}$ and **(b)** $Bi_2O_3:(Sm^{3+}, Li^+)$ samples.

In Fig 3.11 (a), the luminescence intensity increases upon increasing the Sm^{3+} concentration and is found to be maximum for 5 mol% Sm^{3+} doped samples and decreases on further doping due to concentration quenching. The concentration quenching phenomena may arise due to the following reasons-

When the Li concentration exceeds an optimum value, the large amount of produced O^{2-} vacancies tend to create local distortion around Sm^{3+} ions and crystal collapses [50,81,86]. Moreover, the increase in Urbach energy for SL3 sample increases the amount of defect states or disorders in the lattice, thereby increasing the concentration of inactive quenching centres and leads to an increment in the probability of non-radiative transitions, which in turn reduces the luminescence intensity [60].

3.4.6.1 Role of Li^+ ions in luminescence enhancement

The effect of Li^+ co-doping was studied for the optimized Sm^{3+} concentration and it was found that the emission intensity augmented up to 1 mol% and decreased on further doping due to concentration quenching (Fig. 3.11 (b)). The augmentation in intensity is ascribed to the following reasons-

(a) A small amount of Li^+ ions play a crucial role in the luminescence enhancement of the phosphors. Owing to its small ionic radius (0.76Å), Li^+ ions can easily incorporate into the host matrix and can occupy either substitutional or interstitial sites, as a result, the local symmetry around the Sm^{3+} ions is broken, and hence the luminescence increases [60]. The degree of distortion from the inversion symmetry around the Sm^{3+} ions in the crystal field environment of the Bi_2O_3 host lattice is measured by asymmetry ratio, and is given by the following formula [87],

$$A_{asy} = \frac{\text{peak area under the electric dipole transition}}{\text{peak area under the magnetic dipole transition}} \qquad (3.5)$$

It was found that the values of A_{asy} for S5 and SL1 are 1.22 and 1.34, respectively, which suggests that the Li^+ co-doping severely breaks the local crystal field symmetry around the Sm^{3+} ions and enhances the luminescence intensity [80].

(b) From the observed XRD results, as shown in Table 3.1, we infer that the co-doping of Li^+ ions in the Sm^{3+} doped Bi_2O_3 samples increases the crystallite size, and hence, crystallinity is improved, which further reduces the surface to volume ratio. Consequently, the available defect (or quenching) centres present at the surface are reduced, which in turn reduces the probability of non-radiative transitions[88]. Furthermore, the HR-SEM results reveal that the average thickness of nano-sheets increases upon Li^+ co-doping thereby increasing the number of adsorbed unoccupied oxygen sites created over the surface of nano-sheets and hence the available luminescence quenching centers are reduced, which may lead to the enhancement of PL emission intensity[80,81].

(c) Moreover, the reduced microstrain reduces the crystal defects and increases the crystal ordering, which further improves the emission intensity[89]. Fig. 3.12 depicts the plot of

schematic energy level diagram of Sm^{3+} ion, representing all probable transitions involved in the excitation and emission processes.

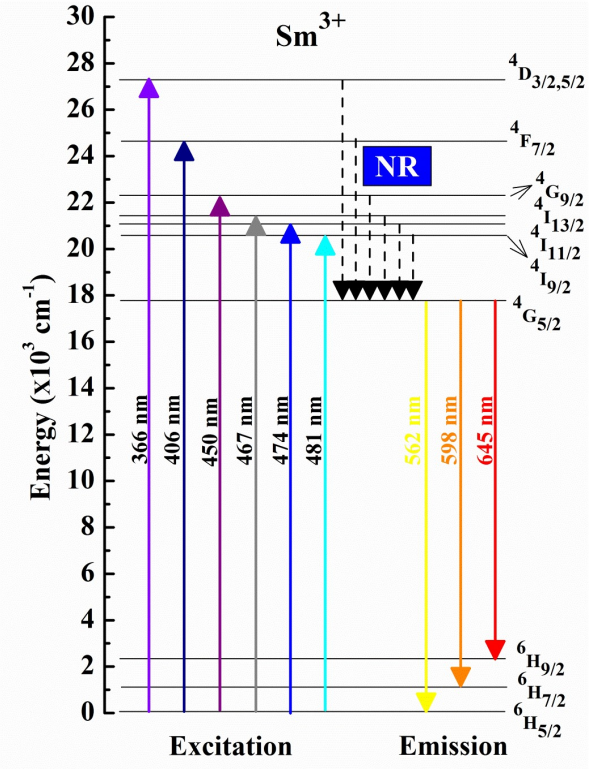

Fig. 3.12 Schematic energy level diagram of Sm^{3+} ion.

3.4.7 CIE and CCT studies

The chromaticity diagram and Commission Internationale de l'Elcairage (CIE) Coordinates of the samples S5 and SL1, calculated from PL emission spectra over the range of 540 - 740 nm under an excitation wavelength of 481 nm are depicted in Fig. 3.13. The calculated values of CIE coordinates for S5 and SL1 are (0.499, 0.498) and (0.524, 0.473), respectively. An evident redshift is observed from the CIE diagram upon Li^+ co-doping in Sm^{3+} doped Bi_2O_3 nano-sheets. Moreover, the correlated color temperature (CCT) values for S5 and SL1 are 2808K and 2397K, respectively. This shows that the radiation temperature corresponding to SL1 is much lower than that of S5

and hence, corroborates that the Li^+ co-doped samples are more suitable for warm wLEDs.

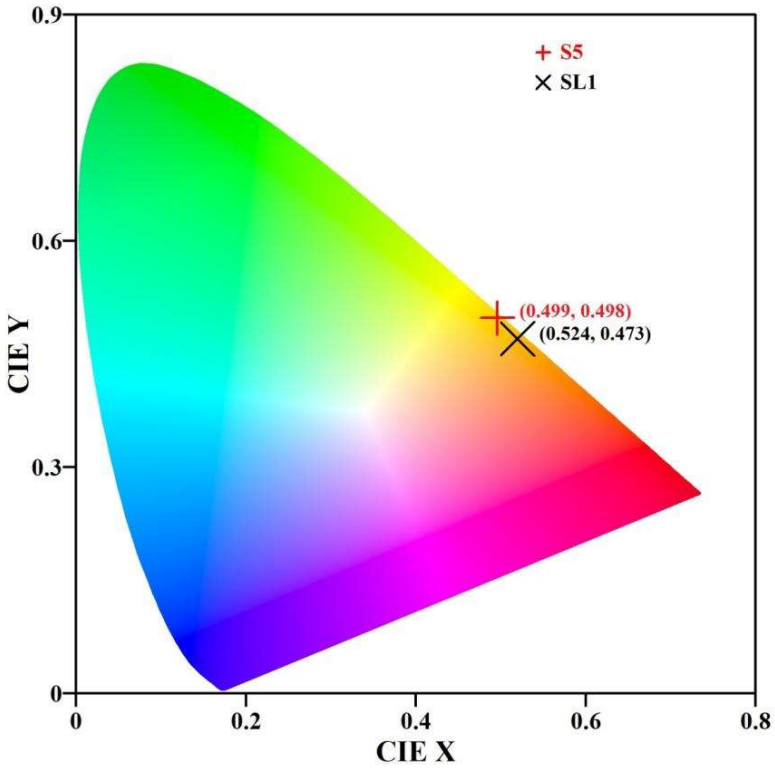

Fig. 3.13 CIE diagram for S5 and SL1.

3.5 Conclusions

In a nutshell, undoped and Sm^{3+}/Li^+ co-doped Bi_2O_3 nanosheets were successfully synthesized by a facile and cost-effective co-precipitation method. The XRD and FTIR results were used as probes for phase quantification and chemical bonding authentication of the samples. The XPS analysis provides the oxidation state and confirms the presence of all elements in the sample. Moreover, it validates the presence of oxygen vacancies in the samples. UV-Vis absorption spectroscopy was used as a tool to investigate the optical band gap and Urbach energy of the samples. Furthermore, HR-SEM along with EDX

analysis was carried out for the surface morphology analysis, elemental confirmation as well as to validate their estimated contents in the samples. PL studies of the samples clearly indicate an augmentation in the emission intensity in the co-doped samples and the CIE and CCT analysis confirm their applicability as phosphors for warm white light emitting diodes.